Particle Inertia Effects on Radar Doppler Spectra Simulation

Zeen Zhu[1], Pavlos Kollias[1,2] and Fan Yang[1]

[1]Environmental and Climate Sciences Dept, Brookhaven National Laboratory, Upton, NY, USA

[2] Division of Atmospheric Sciences, Stony Brook University, Stony Brook, NY, USA

Correspondence to: Zeen Zhu (zzhu1@bnl.gov)

Abstract. Radar Doppler spectra observations provide a wealth of information about cloud and precipitation microphysics and dynamics. The interpretation of these measurements depends on our ability to simulate these observations accurately forward. The effect of small-scale turbulence on the radar Doppler spectra shape has been traditionally treated by implementing the convolution process on the hydrometeor reflectivity spectrum and environment turbulence. This approach assumes that all the particles in the radar sampling volume respond the same to turbulent scale velocity fluctuations and neglects the particle inertial effect. Here, we investigate the inertia effects of liquid phase particles on the forward modelled radar Doppler spectra. A physics-based simulation is developed to demonstrate that big droplets, with large inertia, are unable to follow the rapid change of velocity field in a turbulent environment. These findings are incorporated to a new radar Doppler spectra simulator. Comparison between the traditional and the newly formulated radar Doppler spectra simulators indicates that the conventional simulator leads to an unrealistic broadening of the spectrum, especially in strong turbulence environment. This study provides clear evidence to illustrate the droplets inertial effect on radar Doppler spectrum and develops a physics-based simulator framework to accurately emulate the Doppler spectrum for a given Droplet Size Distribution in turbulence field. The proposed simulator has various potential applications for the cloud/precipitation studies and provides a valuable tool to decode the cloud microphysical and dynamical properties from Doppler radar observation.

1 Introduction

The radar Doppler spectrum represents the frequency (velocity) distribution of the backscattered radar signal at a particular range. For a vertically pointing radar, the Doppler spectrum provides the distribution of the backscattered signal over a range of Doppler velocities, whose value depends on the dynamical (i.e., vertical air motion) and cloud microphysical (i.e., hydrometeors concentration and sizes) properties within the radar sampling volume. A variety of research applications that utilize the full radar Doppler spectrum have been developed. For instance, Doppler spectrum can be used to retrieve rain Droplet Size Distribution (DSD) (Atlas et al., 1973), remove clutters and identify hydrometeor signals (Williams et al., 2018;Luke et al., 2008;Moisseev and Chandrasekar, 2009), identify drizzle development stage (Zhu et al., 2022;Acquistapace et al., 2019), retrieve vertical air motion (Kollias et al., 2002;Williams, 2012;Zhu et al., 2021), characterize the melting-layer properties (Li and Moisseev, 2020;Mróz et al., 2021), and to improve the representation of cloud microphysical process in model (Kollias et al., 2011b). Combined with the depolarization capability, Doppler spectrum can also be used for cloud-phase classifications and to investigate ice-cloud microphysical process (Luke et al., 2010;Luke et al., 2021;Kalesse et al., 2016;Oue et al., 2018). The forward Doppler spectra simulator can further be utilized to simulate radar observation from the modeling output to evaluate the model performance (Oue et al., 2020;Mech et al., 2020;Silber et al., 2022). The list of widely application of the Doppler spectrum in the cloud-precipitation research mentioned above is by no means exhaustive.

Despite the extensive applications, an unambiguous interpretation of radar Doppler spectrum still remains a challenging task in the cloud radar community. One important reason is a lack of full understanding of the entanglement between the hydrometeor microphysics and environment dynamics as well as their manifestation on the Doppler spectrum morphology (Kollias et al., 2002). More specifically, the Doppler spectrum width is mainly contributed by the spread of the still-air hydrometeor terminal velocity, the horizontal and vertical wind shear within the radar observation volume and the environment turbulence; while the Doppler frequency shift is a combined measure of the air motion and the particles falling velocity (Doviak, 2006). A successful separation of the microphysical and dynamical contributions to Doppler spectrum is essential to reduce retrieval uncertainties and to better characterize the cloud-precipitation properties (Zhu et al., 2021).

63   Doppler spectrum simulators have been invaluable for the interpretation of the radar

64   Doppler spectrum shape (Capsoni et al., 2001;Oue et al., 2020;Kollias et al., 2011a;Maahn et al.,

65   2015). Traditionally, the impact of turbulence on the shape of the radar Doppler spectrum is

66   represented by the convolution of the still air (no air motion) hydrometeor reflectivity spectrum

67   with a Gaussian distribution (Gossard and Strauch, 1989). The width of the Gaussian distribution

68   is parameterized as a function of the radar parameters and the turbulence intensity often

69   represented in terms of eddy dissipation rate (Borque et al., 2016). This approach is only valid

70   under the assumption that the droplet inertia effect is negligible and droplets with different sizes

71   can follow exactly the environment wind field. In reality, however, big droplets with large inertia

72   cannot follow the rapid change of wind velocity field unlike small droplets perform (Yanovsky,

73   1996;Lhermitte, 2002). Not accounting for the particle inertia effect can lead to a misinterpretation

74   of the Doppler spectrum and cause large uncertainties for retrieval products (Nijhuis et al., 2016).

75   Several physics-based frameworks have been proposed to simulate the droplet motions in

76   turbulence field (Khvorostyanov and Curry, 2005;Lhermitte, 2002). Here, the approach proposed

77   by Lhermitte (2002) is used to illustrate the droplets inertial effect and to investigate this effect on

78   the radar Doppler spectrum. In detail, we aim to answer the following questions: 1) How does

79   inertia affect the response of a droplet in a fluctuating turbulent wind field? 2) Is this effect

80   significant on the simulated and observed radar Doppler spectrum? and 3) How can we account

81   for the droplet inertia in radar Doppler spectrum simulators? Building on these investigations, a

82   new approach to generate radar Doppler spectrum is described.

83   The structure of this paper is organized as follows: section 2 describes the physical

84   modeling framework used to simulate the liquid droplet motion and to illustrate the droplets inertia

85   effect in a turbulent environment; section 3 proposes the physics-based Doppler spectrum

86   simulator and compares the emulated spectra to the ones generated from the traditional method;

87   in section 4 one observed Doppler spectrum is used as an illustrative example to compare the

88   Doppler spectrum generated from the two simulators; section 5 concludes the major results of this

89   study and followed by a discussion.

90

91

92

93

2 Droplets inertial effect in a turbulent environment

In this section, a physics-based simulation framework used to illustrate the droplets inertia effect in a turbulent environment is presented. First, we will introduce the equations used to describe the velocity of droplets moving in the air. Then a generated turbulent wind field is applied to the simulation framework to illustrate the droplet inertial effect and the potential implication on the generated Doppler spectrum.

2.1 Motion of droplets in the air

The fundemental dynamical framework of describing the droplets motion in the air is adapted from Lhermitte (2002), p.81. Assuming a liquid droplet with diameter of D, the motion of the droplet in the air can be described as:

$$F - mg = m\frac{dV_D}{dt}$$

(1)

where m is the droplet mass, V_D is the droplet velocity, F is the drag force exerted by wind expressed as:

$$F = \frac{C_d S (V_w - V_D)^2 \rho_a}{2} \cdot \text{sgn}(V_w - V_D)$$

(2)

Where C_d is the wind drag coefficient, ρ_a is air density, S is the droplet cross section normal to wind direction. V_w is wind velocity and $(V_w - V_D)$ indicates droplet velocity with respective to air. In a turbulent environment, V_w cloud be either positive or negative, thus the exerted wind can either accelerate or decelerate the droplet velocity. To this end, the sign function $\text{sgn}(V_w - V_D)$ is included to account for the wind drag force direction.

For spherical droplets, S can be calculated as:

$$S = \frac{\pi D^2}{4}$$

(3)

and droplet mass (m) is calculated as:

$$m = \frac{1}{6}\pi \rho_l D^3$$

(4)

where ρ_l is liquid water density.

121   The only unknown factor is the drag coefficient C_d, which should be derived from

122 experiment. Numerous studies have been conducted to measure the sphere terminal velocity in

123 fluid and estimate C_d as a function of Reynolds number (Re) (Schlichting and Kestin, 1961;Lapple

124 and Shepherd, 1940;Haider and Levenspiel, 1989). However, the derived C_d - Re relationships in

125 the previous studies are applied for rigid spherical particles. For the rain droplets with large

126 diameter, the droplet is distorted and the exerted drag coefficient for a given Re deviates from the

127 rigid sphere. To this end, the drag term of the rain droplet is obtained from the measurement of

128 the terminal velocity of liquid droplets. Here, we adapt the experiment data from Gunn and Kinzer

129 (1949), in which study C_d and Re are estimated for liquid droplets with diameter ranging from 100

130 μm to 5.8 mm. The experiment-derived C_d and Re are shown in Figure 1, we further fit the data

131 with a fifth-degree polynomial (red line) to estimate C_d for a given Re:

132         $logC_d = 1.4277 - 0.8598 \times logRe + 0.0699 \times (logRe)^2 - 0.0023 \times (logRe)^3 -$ (5)

133      $0.0003 \times (logRe)^4 + 0.0013 \times (logRe)^5$

134 Where the Reynolds number Re is represented as:

135 $$Re = \frac{|V_w - V_D|\, D\rho_a}{\mu}$$ (6)

136

137 where μ is the air dynamic viscosity. The values used for ρ_a, ρ_l, and μ are $1.22\ kg\ m^{-3}$,

138 $1000\ kg\ m^{-3}$, $1.81 \times 10^{-5}\ kg\ m^{-1}\ s^{-1}$, corresponding to atmospheric environment of $15^\circ C$ and

139 $1000\ hPa$.

140 Combining (1)-(6), a set of ordinary differential equation is constructed, the droplet velocity (V_D)

141 for a given droplet with diameter D as a function of time can be resolved numerically for a given

142 wind field (V_w).

143

144

145

146

147
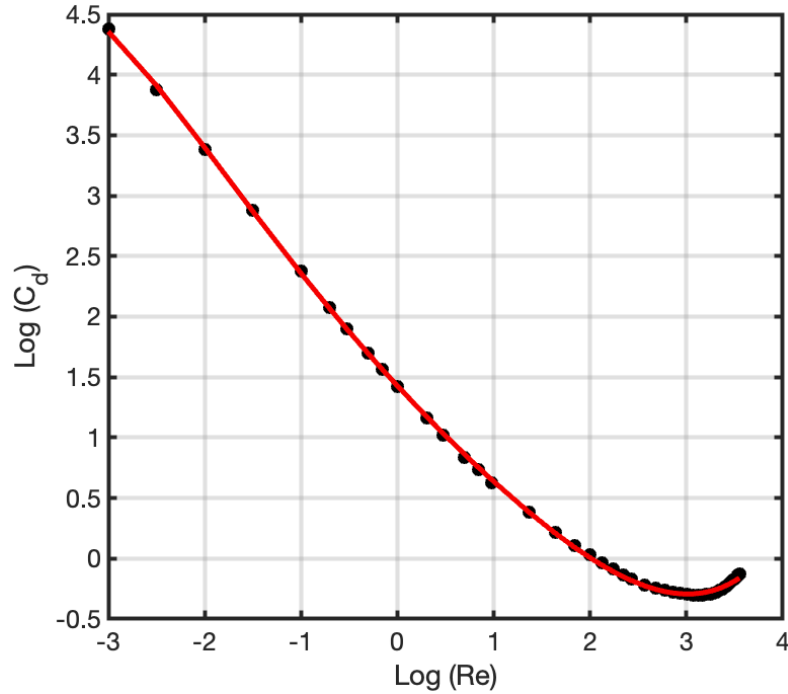
148

149 Figure 1: The black dots represent the experiment-derived C_d and Re adapted from Gunn and

150 Kinzer (1949). The red line is a fifth-degree polynomial fitting function.

151

2.2 Illustration of droplet inertial effect

153 We first illustrate the inertial effect by calculating droplets motion using a constant wind

154 velocity. For simplicity, here we assume all the droplets are moving horizontally, thus the gravity

155 (mg) is neglected in Eq.1. Seven droplets with diameters of 10 μm, 50 μm, 100 μm, 500 μm, 1

156 mm, 2 mm, 5 mm are selected to cover the size range of cloud droplet, drizzle and raindrops.

157 Initial velocity of all the droplets is 0 ms^{-1}, a constant wind velocity with 10 ms^{-1} is exerted upon

158 the droplets when t > 0 s. Due to the wind drag force, droplets start to move but with different

159 accelerations depending on droplet inertia: droplets with small inertia are accelerated more quickly

160 than larger ones. This effect is clearly illustrated in Figure 2: droplet with diameter of 10 μm

161 quickly reach to the wind velocity within only 0.002s, while droplets with 1 mm and 5 mm need

162 5 and 50s to adjust their motion to the exerted wind velocity. The different response time of

163 droplets with different sizes to the exerted wind velocity suggests that small droplets are more

164 capable to follow the velocity variation than their large counterparts.
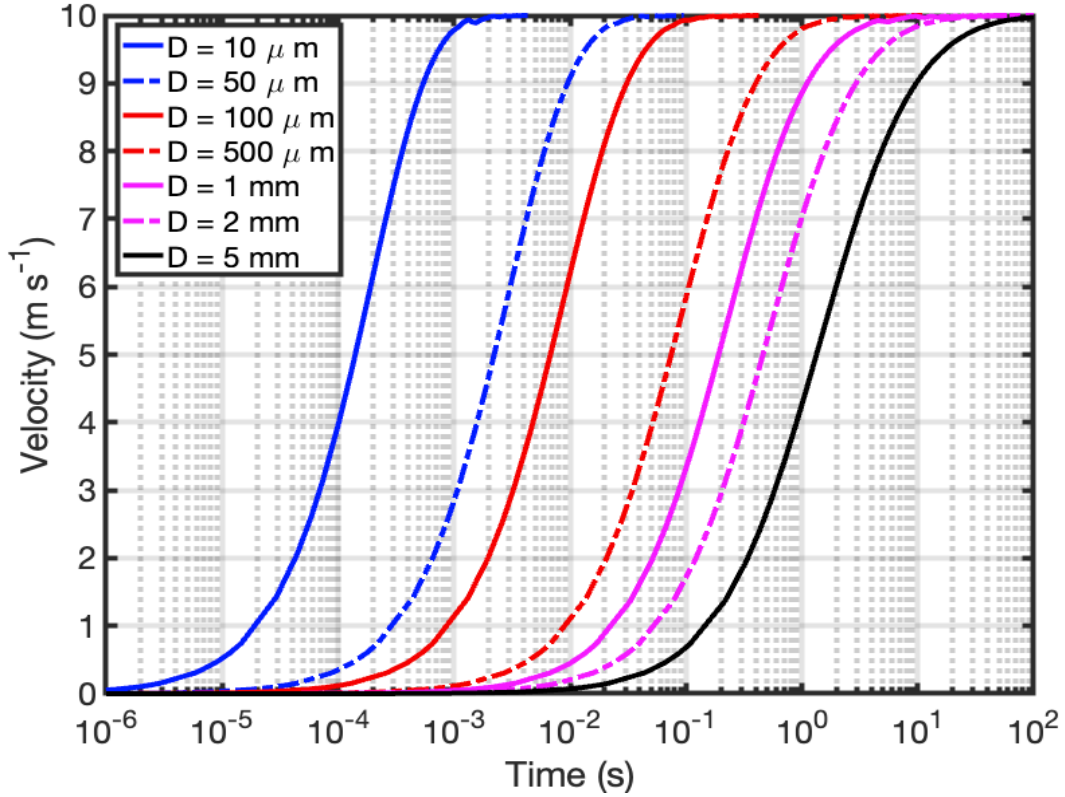
Figure 2. Velocity of droplets with diameter of 10 μm (blue solid line), 50 μm (blue dash-dot line), 100 μm (red line), 500 μm (red dash-dot line), 1 mm (magenta solid line), 2 mm (magenta dash-dot line) and 5 mm (black solid line) as function of time after exerted by a constant wind with 10 ms^{-1} velocity.

In real atmosphere, air velocity is not constant but fluctuates with time as a representative of turbulent nature. In this study we adapt the approach proposed by Deodatis (1996) by using the Spectral Representation Method (SRM) to generate the turbulent wind field based on a predefined Von Karman energy spectrum. The SRM is widely used in the wind engineering community due to its high accuracy, simplicity and computational efficiency. (Shinozuka and Deodatis, 1991;Zhao et al., 2021). Here, the 1-D turbulence wind is generated with 2 Hz sampling frequency, 1000s duration and with standard deviation of 0.3 ms^{-1}, the codes being applied to generate the wind can be accessed from Cheynet (2020). The selection of 0.3 ms^{-1} standard deviation is based on a quantitatively estimation of cloud radar observation under a typical cloudy environment. Specifically, for the convective cloud system with eddy dissipation rate (ε) of 5×10^{-3} m^2 s^{-3} (Mages et al., 2022), the turbulence-contributed Doppler spectrum width (σ_t) from a vertical

181 pointing radar with 30m range resolution(ΔR) and 0.3° beamwidth (θ) at 1km height is estimated

182 to be 0.27 ms⁻¹ based on the equation from Borque et al. (2016):

183

184
$$\varepsilon \approx \frac{\sigma_t^3}{\sigma_z(1.35\alpha)^{3/2}}\left(\frac{11}{15} + \frac{4}{15}z^2\frac{\sigma_x^2}{\sigma_z^2}\right)^{-3/2} \qquad (7)$$

185 Where α is the Kolmogorov constant with 0.5, $\sigma_z = 0.35 * \Delta R$, $\sigma_x = \dfrac{\theta}{4\sqrt{ln2}}$, θ is the one-way

186 half-power width with unit of radian. z is height above surface.

187 The spectrum and time series of the generated air velocity are shown in Figure 3: the

188 turbulence spectrum (Figure 3a) characterizes typical inertial subrange of the turbulence scale with

189 a standard deviation of 0.3 ms⁻¹(Figure 3b).
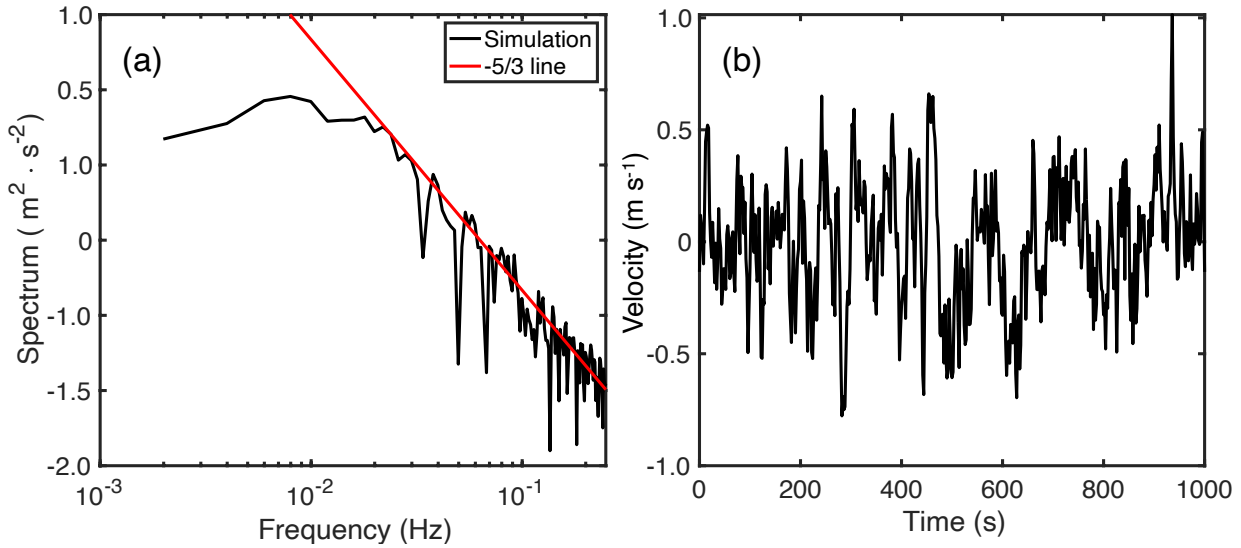
190

191 Figure 3. (a) Spectrum of the simulated turbulence (black line), red line represents the -5/3 slope.

192 (b): Time series of vertical velocity for the simulated turbulence.

193

194 The generated air velocity is assigned to V_w in Eq. (2) to simulate the motion of droplets

195 with initial velocity set as 0 ms⁻¹. Figure 4a shows the time-depended velocity of droplets with

196 selected diameter of 0.5 mm, 1 mm, 2 mm, 3 mm. Droplets with different sizes response

197 differently with the change of wind velocity, and there are two notable characteristics due to the

198 inertial effect (highlighted in the black oval in Fig. 4a). First, large droplets need longer time to

199 adjust to the wind velocity, thus there is a distinct time-lag when the peak velocity is reached for

200 different particles. Second, in addition to the time-lag, the peak velocity reached by the large

201   droplets is smaller than the small droplets. Here, we use correlation coefficient between the actual
202   wind velocity and the droplet velocity to quantify the inertial effect. A correlation coefficient of 1
203   represents droplets can follow exactly the wind velocity and a correlation coefficient less than 1
204   indicates a time-lag effect between the wind and droplet velocity due to droplet inertia. Figure 4b
205   shows that the correlation coefficient is close to 1 when the droplets are smaller than 50 µm but it
206   decreases dramatically as droplet size increases. The correlation coefficient reaches to 0 when
207   diameter reaches to 2000 μm. In addition, for droplets with diameters smaller than 300 μm the
208   standard deviation of the actual droplet velocity is 0.29 ms^{-1} (blue curve, Figure 4b), which is close
209   to standard deviation of the background wind field (0.3 ms^{-1}). As droplet size increases, the
210   velocity variation decreases due to droplet inertial effect.

211   The simulation results shown in Figure 4 suggest that droplets with diameter smaller than
212   300 μm are less affected by inertia and can quickly adjust their velocity to the imposing wind field,
213   and thus, small cloud droplets can be treated as perfect air tracers (Kollias et al., 2001). On the
214   other hand, large droplets (D > 0.5 mm) exhibit a time lag in their response to the air motion and
215   an amplitude reduction (inertia-based filtering). As the observed Doppler velocity is a combined
216   measure of the droplet velocity and the ambient air motion, this droplet inertial effect is expected
217   to have a considerable effect on the generated radar Doppler spectrum. In the following section,
218   we will illustrate how the radar Doppler spectrum is affected by droplet inertia and how to account
219   for this effect using a new radar Doppler spectrum simulator.

220

221

222
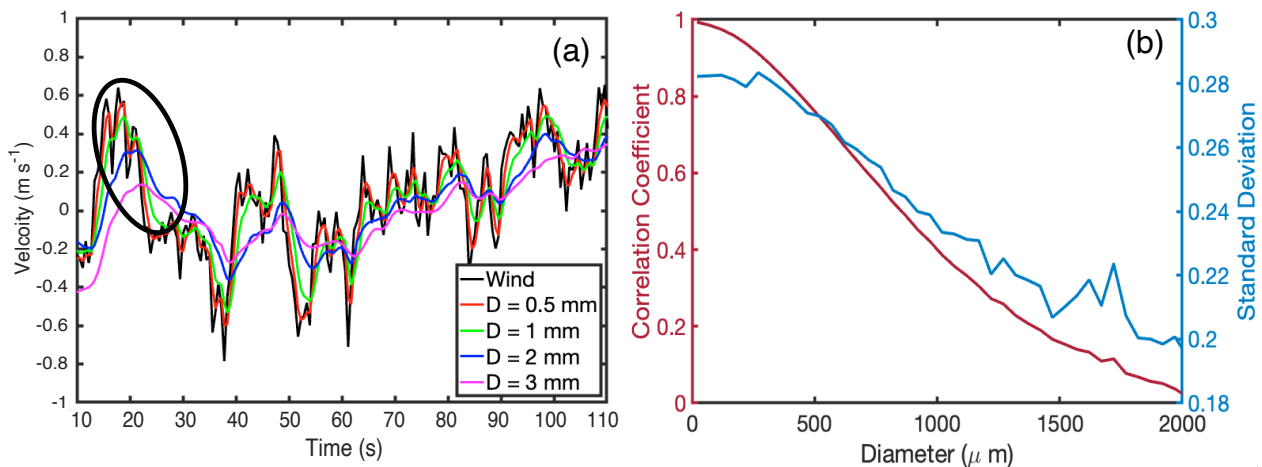
Figure 4. (a) Generated wind velocity field (black line) and the simulated velocity for particles with diameter of $0.5mm$ (red line), $1mm$ (green line), $2mm$ (blue line) and $3mm$ (magenta line) from 10s to 110s. The black oval indicates the period showing droplet inertia effect. (b) Left axis: correlation coefficient between wind field and droplet velocity for different droplets size; right axis: standard deviation of the droplets velocity with different droplets size. Only droplets with size from $0\ \mu m$ to $2000\ \mu m$ are shown for the sake of clarity.

3 Radar Doppler spectrum Simulator

Two methodologies for simulating the radar Doppler spectrum for a given DSD and turbulence conditions are used here. The first approach is the traditional one. All droplets, independent of their sizes, are assumed to have no inertial effects and thus act like perfect tracers. In this case, the radar Doppler spectrum in a turbulent environment is represented through the convolution of a Gaussian distribution and the radar Doppler spectrum in still air which is only determined by the hydrometeor DSD (Gossard, 1981; Kollias et al., 2011, Zhu et al., 2021). A brief overview of the traditional method is described in section 3.1.

3.1 Traditional Doppler spectrum simulator

For a given DSD described by a number concentration $N(D)$ per unit of volume in m⁻⁴, the radar reflectivity $d\eta(D)$ (m²/m³) from particles with diameter between D to $D + dD$ can be expressed as Lhermitte, (2002, p. 228):

$$d\eta(D) = N(D)\sigma_b(D)dD \tag{8}$$

where $\sigma_b(D)$ is the backscatter cross section (m²) of a particle with diameter D in m. Mie scattering theory is used to estimate $\sigma_b(D)$. In this formulation, the radar power spectrum distribution is provided in terms of particle size. Profiling radar do not observe the radar backscatter-energy power spectrum $d\eta(D)$ but the radar Doppler spectrum density $S_q(V_t)$ where V_t is the droplet still-air terminal velocity. The conversion from droplet size to velocity requires a $V_t(D)$ relationship. Here, the function proposed by Lhermitte, (2002, p.120) is used to estimate V_t as a function of droplet diameter (D):

$$V_t(D) = 920 \times (1 - exp(-6.8 \times D^2 - 4.88 \times D)) \tag{9}$$

where the unit of D and V_t is in cm and cms⁻¹ respectively. Subsequently, the radar Doppler spectral density $S_q(V_t)$ in units of m²m⁻³ (ms⁻¹)⁻¹ is given by:

$$254 \qquad S_q(V_t) = \frac{d\eta}{dV_t} = \frac{d\eta}{dD}\frac{dD}{dV_t} = N(D)\sigma_b(D)\frac{dD}{dV_t} \qquad (10)$$

255 where $\frac{dD}{dV_t}$ is estimated from Eq. 9.

256   The $S_q(V_t)$ is the "still-air" radar Doppler spectrum where the only velocity contribution

257 is the droplet still-air terminal velocity . In the real atmosphere, the observed velocities from the

258 radar include the turbulent motions with scales larger or smaller than that of the radar sampling

259 volume (Kollias et al., 2001;Borque et al., 2016). The contribution of turbulence on Doppler

260 spectrum broadening is commonly parameterized as σ_t. It is important to note that the σ_t value

261 also strongly depend on the radar sampling characteristics (Kollias et al., 2005). For the same EDR

262 value, σ_t is lower for radar systems with short time dwell, narrow beamwidth and short pulse

263 length (Borque et al., 2016). The σ_t is typically used to introduce the effect of turbulence on the

264 radar Doppler spectrum. Under the assumption of isotropic turbulence, the distribution of the

265 turbulent motions within the radar sampling volume can be approximated using a Gaussian

266 function:

$$267 \qquad G(v) = \frac{1}{\sigma_t\sqrt{2\pi}} \times \exp\left(-\frac{1}{2}\left(\frac{v}{\sigma_t}\right)^2\right) \qquad (11)$$

268 And its impact on radar Doppler spectrum is formulated by the convolution between $S_q(V_t)$ and

269 *G(v)* (Gossard and Strauch, 1989) as:

$$270 \qquad S(v) = \left(S_q * G\right)(v) = \int_{-\infty}^{\infty} S_q(u)G(v-u)du \qquad (12)$$

271 **3.2 Physics-simulation based Doppler spectrum simulator**

272   In this approach, instead of using a Gaussian distribution to parameterize turbulence field

273 and applying the convolution process to represent the interaction between DSD and environmental

274 turbulence, the radar Doppler spectrum is generated using a large number of simulated droplet

275 velocities during a given simulation period. Specifically, for droplet with diameter of D moving in

276 a turbulent flow, the droplet velocity at each specific time can be numerically resolved as $V(D,t)$

277 based on the ordinary differential equations described in section 2.1.

278   The radar Doppler spectrum density at each time step $S_t(v)$ can be directly estimated as:

$$279 \qquad S_t(v) = \frac{\sum N(D_{V_{i-1}\sim V_i})\sigma_b(D_{V_{i-1}\sim V_i})}{V_i - V_{i-1}} \qquad (13)$$

280 Where $D_{V_{i-1}\sim V_i}$ represents the diameter of the particle with velocity within the predetermined

281 Doppler velocity interval $[V_{i-1}, V_i]$ at each timestep, $N(D_{V_{i-1}\sim V_i})$ and $\sigma_b(D_{V_{i-1}\sim V_i})$ indicate the

282 number concentration and the backscatter power corresponding to each diamater. The
283 predetermined Doppler velocity V_i is depended on the radar configuration of Nyquist velocity
284 ($V_{nyquist}$) and the number of the Fast Fourier Transform points ($NFFT$):

$$V_i = -V_{nyquist} + \frac{2V_{nyquist}}{NFFT} \times i \;;\; i = [1, 2, 3, \dots NFFT] \tag{14}$$

286 The final Doppler spectrum can be obtained by averaging $S_t(v)$ during the simulated period:

$$S(v) = \frac{1}{N_t} \sum_{t=1}^{t=N_t} S_t(v) \tag{15}$$

288 where N_t is the total simulation timesteps:

$$N_t = T \times f \tag{16}$$

290 Where T and f is the simulated time and the sampling frequency of the generated turbulence
291 wind field.

292   It is noted that the emulated radar Doppler spectrum is dependent on the generated
293 turbulence flow, which is contolled by three parameters: time duration (T), sampling frequency (f)
294 and standard deviation (σ). σ quantify the turbulence intensity while T and f determine the total
295 emulated time steps. Here we use the typical cloud radar configurations to guide the choice of T
296 and f. Specifically, T is set as 2s and f is set as 20 Hz to accommodate the cloud radar operated
297 at Atmospheric radiation measurement (ARM) program with approximately 40 spectra being
298 averaged in 2s (Kollias et al., 2005).

299

300 **3.3 Doppler spectra comparison from two simulators**

301   Both simulators described above are applied to emulate the Doppler spectrum observed by
302 a 94-GHz (W-band) profiling cloud radar for a given DSD and for a set of different turbulence
303 environments. The Nyquist velocity is set as $\pm$ 12 ms^{-1} and a 512-point Fast Fourier Transform
304 (FFT) is used to generate the radar Doppler spectrum. The Marshall-Palmer exponential DSD
305 (Marshall and Palmer, 1948) with $N(D) = N_0 e^{-\Lambda D}$ is used to represent the DSD in the radar
306 sampling volume. The values of the intercept parameter N_0 and the slope factor Λ are chosen to be
307 $0.08 \; cm^{-4}$ and $15 \; cm^{-1}$. Droplet diameter ranges 10 to 4000 μm with bin size as 1 μm. The
308 selection of W-band radar and the use of a rain DSD is because it is well known that the W-band
309 radar Doppler spectrum in rain has distinct features which allow to pinpoint the Doppler spectrum
310 morphology. Specifically, according to the Mie scattering theory, radar backscattering cross

311 section varies in an oscillatory manner with particle size (Mie, 1908). With the 3.2 mm wavelength

312 radar, the backscattering cross section as a function of droplet size is characterized as several local

313 minimal values with diameter of 1.66, 2.86 mm, which are corresponding to still-air terminal fall

314 velocity of 5.83, 7.89 ms^{-1}. This unique feather is known as "Mie notches" in the radar Doppler

315 spectrum (Kollias et al., 2002;Kollias et al., 2007;Courtier et al., 2022). In the simulation,

316 turbulence field is generated with 20 Hz frequency (f),100s duration (T) and standard deviation

317 (σ) of 0.05 ms^{-1}, 0.25 ms^{-1}, 0.35 ms^{-1}and 0.45 ms^{-1}, respectively.The reason of applying different

318 turbulence settings is to better illustrate the droplet inertia effect under different turbulence

319 environment. It is expected that with increasing turbulence intensity the droplet inertia effect will

320 be manifested in larger differences between the generated radar Doppler spectrum from two

321 methods.

322   When solving the ordinary differential equations described in Section 2.1, the initial droplet

323 velocity is set as 0 ms^{-1}, thus at the beginning of the simulation the droplet gravity force is greater

324 than the wind drag force, the droplet will accelerate until their terminal fall velocity is reached,

325 after which the droplets fluctuate around the terminal fall velocity with variations induced by the

326 exerted wind. The radar Doppler spectrum should be estimated after the steady state is reached.

327 Here, we split the 100s simulated period to two parts: the first 40s is the "speed-up" time which

328 allows the droplets of different size adjust to their steady state, the remaining 60s is used for

329 Doppler spectrum emulation. Specifically,each Doppler spectrum is estimated within a 2s interval

330 as illustrated in Section 3.2, then the generated 30 Doppler spectra in the 60s are further averaged

331 to produce the final Doppler spectrum. This final average step is used to smooth the Doppler

332 spectrum generated in a short period (2s) during which the averaged exerted wind may have a non-

333 zero value.

334   The emulated Doppler spectrum from two methods with four turbulence settings are shown

335 in Figure 5. In a turbulent environment with σ_t of 0.05 ms^{-1} (Figure 5a), the two simulated spectra

336 (red and blue line in Figure 5a) and the Doppler spectrum without turbulence broadening (black

337 line) are almost overlapping with each other, indicating that the radar Doppler spectrum shape is

338 dominated by the DSD shape and the droplets still-air terminal fall velocity in weak turbulence

339 conditions. For σ_t equal to 0.25 ms^{-1}, the broadening of the right edge of the radar Doppler

340 spectrum from the physics-based simulation(PBS) approach (red line in Figure 5b) is less than that

341 produced with the convolution approach (blue line in Figure 5b). As σ_t increases to 0.35 ms^{-1}, a

342 large differences between the right edges of the spectra from the two simulators can be clearly

343 identified. When σ_t reaches to 0.45 ms^{-1}, the right edge velocity difference between two spectra is

344 larger than 1 ms^{-1}. Overall, the right edge from the PBS-generated Doppler spectrum is more steep

345 than that from the covolution-based approach, illustrating that large droplets can not follow the

346 rapidly changed turbulent field due to the inertia effect. Another notable finding is the left part of

347 Doppler spectra (velocity smaller than 4 ms^{-1}) from two simulators almost overlap with each other

348 in different turbulence scenarios, as this part of the spectrum is mostly contributed by small

349 droplets with negligible inertial effect, thus the corresponding Doppler spectrum can be adequately

350 represented by the convolution process.
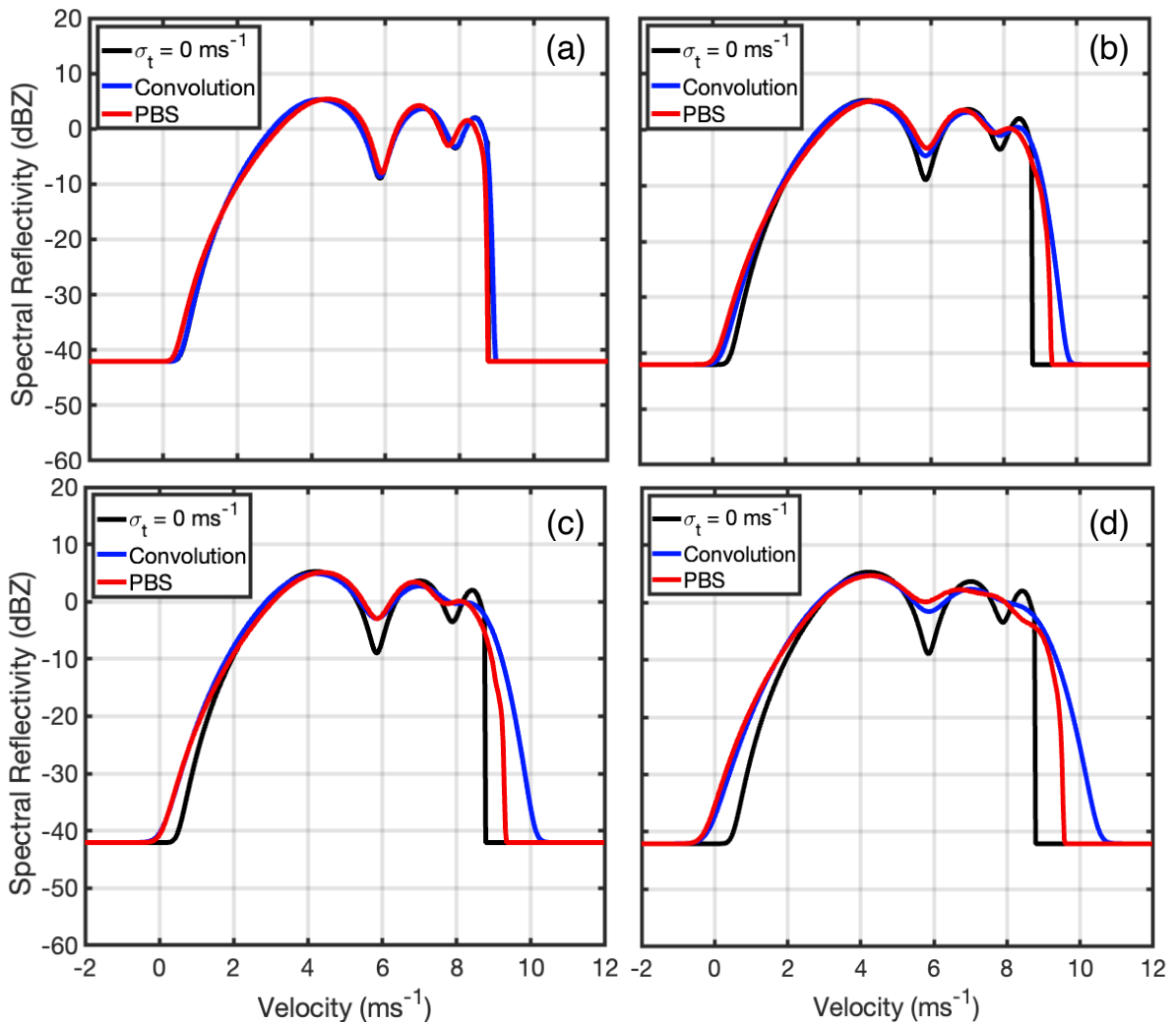
351

352 Figure 5. Doppler spectrum generated by the convolution-based (blue line) and physics-based

353 simulation (PBS) (red line) approach for turbulence standard deviation with (a) 0.05 ms^{-1}, (b) 0.25

354   ms^{-1}, (c) 0.35 ms^{-1}, (d) 0.45 ms^{-1}. The black line represents generated Doppler spectrum with $\sigma_t =$

355   0 ms^{-1}. Positive velocity indicates downward motion.

356

357   Comparing the three generated Doppler spectra in Figure 5, we can clearly identify the

358   effect of droplet inertia on Doppler spectrum morphology under different turbulence environments.

359   In general, both simulators indicate a wider Doppler spectrum under a large turbulence condition,

360   but with different broadening magnitudes. The convolution-based approach generates a wider

361   spectra in a more turbulent environment. This overestimation of the turbulence broadening effect

362   indicates that the convolution process used in the conventional simulator is unable to accurately

363   represent the interaction between DSD and turbulence field. On the other hand, for the small

364   droplets, the inertial effect is negligible and the generated Doppler spectra from two approaches

365   are consistent with each other. It is therefore concluded that the convolution process can simulate

366   the Doppler spectrum for the light drizzle precipitation which mostly occurs in marine boundary

367   layer clouds but it is inadequate to emulate Doppler spectrum for the heavy precipitation in deep

368   convection, especially in the presence of strong turbulence environment.

369

370   **4 An illustrative example of Doppler spectrum comparison between observation and**

371   **simulation**

372   In this section, we will present an illustrative example by using one observed Doppler

373   spectrum to evaluate the performance of the simulators. The observed Doppler spectrum is

374   obtained from the W-band ARM Cloud Radar (WACR) at the ARM Southern Great Plain (SGP)

375   observatory during a heavy precipitation period on May 9, 2007. For the WACR, the maximum

376   unambiguous velocity is 7.8ms^{-1}, which is smaller than the still-air terminal velocity of droplets

377   with diameter larger than 3mm and lead to velocity folding. Here velocity de-aliasing process is

378   performed to reconstruct the Doppler spectrum with velocity from 0 ms^{-1} to 11 ms^{-1}. The observed

379   Doppler spectrum is further calibrated from the displacement caused by vertical air motion by

380   pinpointing the location of first Mie notch of the Doppler spectrum to 5.83ms^{-1}.(Kollias et al.,

381   2002). To simulate the Doppler spectrum, the hydrometeor DSD and the turbulence broadening

382   term (σ_t) are needed. Here, the raindrops DSD is observed from the impact disdrometer which can

383   measure droplet diameter from 0.3mm to 5.4 mm with 20 bins (Wang et al., 2021). The temporal

384   resolution of the WACR and the disdrometer is 4.28s, 1min respectively. To make the observation

385   from two instruments comparable, the WACR-observed Doppler spectra are averaged over 1min

386   to coincide with the disdrometer observational period. For this example, we use the disdrometer-

387   measured DSD from 05:44 to 05:45 UTC to simulate the radar Doppler spectrum and compare it

388   with the one observed of WACR in the same period.

389   The observed DSD is shown in Figure 6a, and the corresponding WACR-observed Doppler

390   spectrum is shown as the black line in Figure 6b. Based on the observed DSD, the radar Doppler

391   spectrum for the droplets falling in still air is generated (not shown), from which the DSD-

392   contributed Doppler spectrum width (σ_D) is estimated as 1.34 ms^{-1}. Since the wind shear

393   broadening contribution (σ_S) to radar Doppler spectrum is generally smaller than σ_D and the

394   turbulence broadening (σ_t) (Borque et al., 2016), here we neglect the σ_S contribution and estimate

395   σ_t as:

396

$$\sigma_t^2 = \sigma_O^2 - \sigma_D^2$$

397   Where σ_O is the observed Doppler spectrum width, which is 1.46 ms^{-1} in this example, and

398   σ_t is estimated as 0.58 ms^{-1}. To estimate the accuracy of σ_t, we further assume the observed DSD

399   is the only source of the uncertainty. Considering that the accuracy of the droplets size

400   measurement of the disdrometer is approximately ±5% (Wang et al., 2021), the uncertainty of σ_D

401   and σ_t is estimated as 0.15 ms^{-1}.

402   With the observed DSD and the estimated σ_t, the radar Doppler spectrum can be simulated.

403   It is noted that large rain droplets falling in the air are nonspherical, thus backscattered power from

404   an oblate droplet may be different from the one from rigid liquid sphere. To this end, for the Mie

405   scattering calculation, axis ratio ($\frac{a}{b}$) of the droplet with diameter largher than 2mm is considered

406   as a function of diameter (*D*) with unit of *mm* (Pruppacher and Beard, 1970):

407

$$\frac{a}{b} = 1.03 - 0.062D$$

408   The simulated Doppler spectrum from the convolution and the PBS method are shown in

409   Figure 6(b). It is noticeable that the Doppler spectrum from the PBS approach (red line) is more

410   noisy than that from the convolution approach (blue line). This is due to the insufficient bin

411   categories of the particle measured from disdrometer, it is expected that with increasing the number

412   of measured particle size, the generated Doppler spectrum become more smooth. Nevertheless, it

413   is still recognizable that the both the morphology and the magnitude of the PBS-based spectrum

414   right edge is more consistent with observation compared with the one generated from the

415 convolution approach. Both of the two simulators represent the first peak of the Doppler spectrum
416 from 3 ms^{-1} to 6 ms^{-1} very well, while neither of them generate a consistent second peak
417 morphology compared with observation. The left edge of the Doppler spectrum from the
418 convolution-based approach is broader than the observation, while the PBS is unable to represent
419 the Doppler spectrum smaller than 1ms^{-1} due to the abscent of the droplets with diameter smaller
420 than 0.3 *mm* observed from disdrometer.

421 The purpose of this Doppler spectrum comparison is not for a robust validation but used as
422 an illustrative example to show the morphology of the simulated Doppler spectrum based on real
423 observations and to discuss the required measurements would be used for robust Doppler spectrum
424 simulator validation. To a certain degree, a more consistency Doppler spectrum morphology is
425 identified between the observation and from the PBS simulator, especially for the right edge of the
426 spectrum. However, great cautions should be taken for further interpretation as both of the
427 simulators cannot represent the left part of the Doppler spectrum and the second notches very well.
428 This discrepancy is mainly because the observed DSD by disdrometer may not an adequate
429 representation of the hydrometeors that contribute the Doppler spectrum observed by WACR.
430 Specifically, there are three critical challenging issues should be overcome before a solid and
431 convincing Doppler spectrum simulator evaluation effort being performed: 1) the disdrometer is
432 located at the surface, while the lowest measurement height of WACR is 460m. When the rain
433 droplets fall, droplets may collide, breakup, and being advected from adjacent regions by the
434 horizontal wind; Thus a large uncertainty is expected by using the surface-observed DSD to
435 represent the hydrometeor distribution at 450m above; 2) the observed DSD from the disdrometer
436 only measure droplets with 20 size categories, which is insufficient for the physics-based
437 simulation to generate a smooth and complete Doppler spectrum; 3) the uncertainty of the
438 estimated σ_t is challenging to be well constrained due to the large uncertainty of the observed DSD
439 mentioned above. A comprehensive and solid validation of the Doppler spectrum simulator require
440 simultaneous and well- aligned DSD and Doppler spectrum measurement; large number of the
441 measured droplet size categories and carefully estimation of the environment turbulence
442 broadening factors.

443
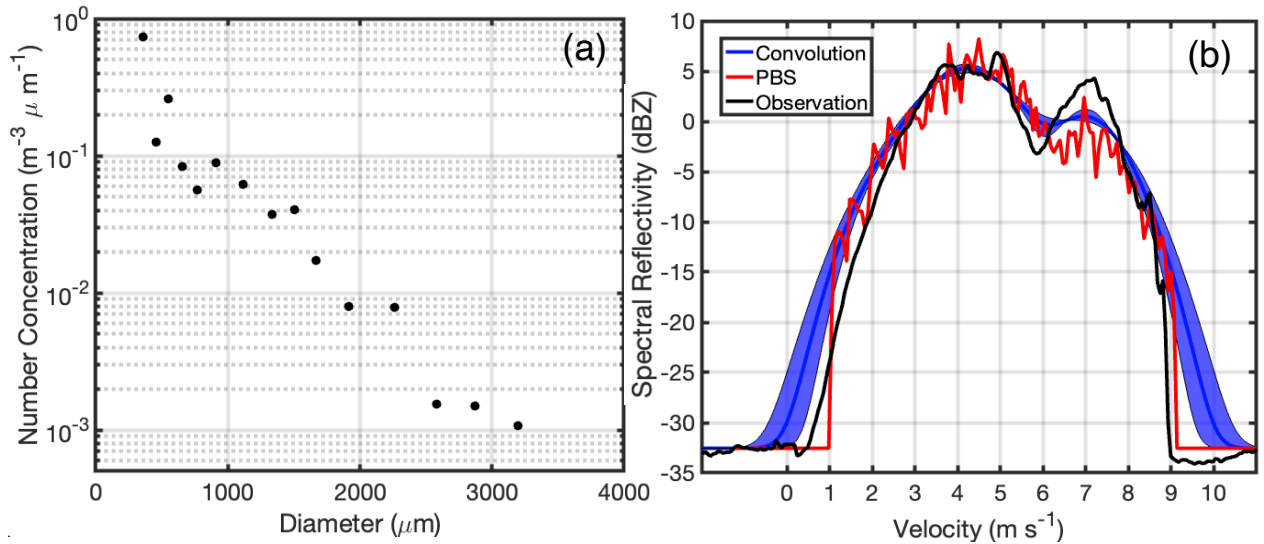
Figure 6. (a) Black dots represent the observed raindrop number concentration from disdrometer at 05:44 (UTC) on May 9, 2007 on SGP site. (b) Doppler spectra simulated from the PBS (red) and convolution (blue) method and the observed spectrum from WACR (black line). The blue shaded region represents the uncertainty of the simulated Doppler spectrum produced by the uncertainty in σ_t based on the convolution method. Positive velocity indicates downward motion.

5 Conclusions

The radar Doppler spectrum offer unprecedent capabilities for studying cloud and precipitation microphysics. Recent advancements in radar technology and signal processing have enable the continuous recording of high-quality radar Doppler spectra observations from a wide range of profiling radar systems (Kollias et al., 2005;Kollias et al., 2016). Until now, the simulation of the radar Doppler spectra was based on well-established techniques (Gossard, 1988;Kollias et al., 2011a). However, inertial effect of large droplets are typically neglected in the design of current simulators. Here, the impact of the liquid droplet's inertia on the shape of the radar Doppler spectrum was investigated. A physics-based simulation framework is developed to simulated the droplets velocity in a given turbulence environment. It demonstrates that big droplets with large inertia will take longer time to adapt to the change of velocity field, indicating large droplets are incapable of following the turbulence wind as small droplets do.

Building on the simulation framework, a new approach is proposed to emulate Doppler spectrum by simulating the velocity of each droplet during the entire time domain. The simulated

W-band radar Doppler spectrum is compared with the one generated from the traditional method for a typical DSD with four different turbulence environments. The comparison indicates that the traditional Doppler simulator without considering the inertial effect generates an artificially broader Doppler spectrum. This inertia effect becomes more noticeable as turbulence intensity increases. This finding suggests that special caution should be taken when applying convolution-based approaches to represent DSD-turbulence interaction in heavy precipitation. In the case of light precipitation mostly happening in marine boundary layer cloud, the droplet inertia effect on Doppler spectrum is negligible and the traditional simulator generates consistent results with the proposed simulator.

One WACR-observed Doppler spectrum collected from the ARM SGP observatory is compared with the simulated Doppler spectrum as an illustrative example to validate the fidelity of the simulator from the convolution and the PBS-based approach. The presented case shows that the proposed PBS generate a more similar morphology of the right edge of the Doppler spectrum compared with the traditional simulator. However, both of two simulator fail to reconstruct the left edge and the second notch of the Doppler spectrum. These inconsistents are due the fact that the surface-based DSD from disdrometer is inadequate to represent the hydrometeor observed by cloud radar at a high level. A careful and solid validation of the radar Doppler spectrum simulator would require co-aligned observations of DSD and Doppler spectrum and well-constrained turbulent broadening estimations. Nevertheless, the proposed Doppler spectrum simulator, with the ability to simulate individual droplet motion as well as their manifestation on Doppler spectrum, provide an valuable tool to improve the understanding of Doppler radar observation from a fundemental physics perspective. We expect this proposed Doppler spectrum simulation framework can stimulate more studies to better interpret the Doppler radar observation and to decode the microphysics and dynamics information concealed in radar Doppler spectrum.

Competing interests.

P. K. is the associate editor of AMT and the peer-review process was handled by an independent editor. The authors have no other competing interests to declare.

Code/Data availability

The codes of the proposed Doppler spectrum simulator can be accessed via https://doi.org/10.5281/zenodo.7897981.

Ground-based data were obtained from the Atmospheric radiation measurement (ARM) user facility, a U.S. Department of Energy (DOE) Office of Science user facility managed by the Office of Biological and Environment Research.

W-Band (95 GHz) ARM Cloud Radar (WACRSPECCMASKCOPOL). 2007-05-09 to 2007-05-10, Southern Great Plains (SGP) Central Facility, Lamont, OK (C1). Compiled by K. Johnson, D. Nelson and A. Matthews. ARM Data Center. Data set accessed 2022-07-05 at http://dx.doi.org/10.5439/1025318.

Impact Disdrometer (DISDROMETER). 2007-05-09 to 2007-05-10, Southern Great Plains (SGP) Central Facility, Lamont, OK (C1). Compiled by D. Wang. ARM Data Center. Data set accessed 2022-07-05 at http://dx.doi.org/10.5439/1025181.

Author contributions

Zeen Zhu implemented the method, performed the analysis, produced the figures, and wrote the initial draft of the manuscript. Pavlos Kollias supervised and provided advice and guidance on all aspects of the analysis and contributed to the writing of the manuscript. Fan Yang advised on results interpretation and manuscript editing. All authors read the manuscript draft and contributed comments.

Financial support

Zeen Zhu's contribution is supported by Brookhaven National Laboratory via the Laboratory Directed Research and Development Grant LDRD 22-054. Pavlos Kollias and Fan Yang are supported by the US Department of Energy (DOE) under contract DE-SC0012704.

Reference

Acquistapace, C., Löhnert, U., Maahn, M., and Kollias, P.: A New Criterion to Improve Operational Drizzle Detection with Ground-Based Remote Sensing, Journal of Atmospheric and Oceanic Technology, 36, 781-801, 2019.

Atlas, D., Srivastava, R., and Sekhon, R. S.: Doppler radar characteristics of precipitation at vertical incidence, Reviews of Geophysics, 11, 1-35, 1973.

Borque, P., Luke, E., and Kollias, P.: On the unified estimation of turbulence eddy dissipation rate using Doppler cloud radars and lidars, Journal of Geophysical Research: Atmospheres, 121, 5972-5989, 2016.

Capsoni, C., D'Amico, M., and Nebuloni, R.: A multiparameter polarimetric radar simulator, Journal of Atmospheric and Oceanic Technology, 18, 1799-1809, 2001.

Cheynet, E.: Wind field simulation (text-based input), Zenodo, Tech. Rep., 2020, doi: 10.5281/ZENODO. 3774136, 2020.

Courtier, B. M., Battaglia, A., Huggard, P. G., Westbrook, C., Mroz, K., Dhillon, R. S., Walden, C. J., Howells, G., Wang, H., and Ellison, B. N.: First Observations of G‑Band Radar Doppler Spectra, Geophysical Research Letters, 49, e2021GL096475, 2022.

Deodatis, G.: Simulation of ergodic multivariate stochastic processes, Journal of engineering mechanics, 122, 778-787, 1996.

Doviak: Doppler radar and weather observations, Courier Corporation, 2006.

Gossard, E. E.: Measuring drop-size distributions in clouds with a clear-air-sensing Doppler radar, Journal of Atmospheric and Oceanic Technology, 5, 640-649, 1988.

Gossard, E. E., and Strauch, R. G.: Further guide for the retrieval of dropsize distributions in water clouds with a ground-based clear-air-sensing Doppler radar, NASA STI/Recon Technical Report N, 90, 11911, 1989.

Gunn, R., and Kinzer, G. D.: The terminal velocity of fall for water droplets in stagnant air, Journal of Atmospheric Sciences, 6, 243-248, 1949.

Haider, A., and Levenspiel, O.: Drag coefficient and terminal velocity of spherical and nonspherical particles, Powder technology, 58, 63-70, 1989.

Kalesse, H., Szyrmer, W., Kneifel, S., Kollias, P., and Luke, E.: Fingerprints of a riming event on cloud radar Doppler spectra: observations and modeling, Atmospheric Chemistry and Physics (Online), 16, 2016.

Khvorostyanov, V. I., and Curry, J. A.: Fall velocities of hydrometeors in the atmosphere: Refinements to a continuous analytical power law, Journal of the atmospheric sciences, 62, 4343-4357, 2005.

Kollias, Albrecht, B. A., Lhermitte, R., and Savtchenko, A.: Radar observations of updrafts, downdrafts, and turbulence in fair-weather cumuli, Journal of the atmospheric sciences, 58, 1750-1766, 2001.

Kollias, Clothiaux, E. E., Albrecht, B. A., Miller, M. A., Moran, K. P., and Johnson, K. L.: The atmospheric radiation measurement program cloud profiling radars: An evaluation of signal processing and sampling strategies, Journal of Atmospheric and Oceanic Technology, 22, 930-948, 10.1175/jtech1749.1, 2005.

567   Kollias, Clothiaux, E., Miller, M., Albrecht, B., Stephens, G., and Ackerman, T.: Millimeter-
568   wavelength radars: New frontier in atmospheric cloud and precipitation research, Bulletin of
569   the American Meteorological Society, 88, 1608-1624, 2007.
570   Kollias, Remillard, J., Luke, E., and Szyrmer, W.: Cloud radar Doppler spectra in drizzling
571   stratiform clouds: 1. Forward modeling and remote sensing applications, Journal of Geophysical
572   Research-Atmospheres, 116, 10.1029/2010jd015237, 2011a.
573   Kollias, Szyrmer, W., Remillard, J., and Luke, E.: Cloud radar Doppler spectra in drizzling
574   stratiform clouds: 2. Observations and microphysical modeling of drizzle evolution, Journal of
575   Geophysical Research-Atmospheres, 116, 10.1029/2010jd015238, 2011b.
576   Kollias, P., Albrecht, B. A., and Marks, F.: Why Mie? Accurate observations of vertical air
577   velocities and raindrops using a cloud radar, Bulletin of the American Meteorological Society,
578   83, 1471-1483, 10.1175/bams-83-10-1471, 2002.
579   Kollias, P., Clothiaux, E. E., Ackerman, T. P., Albrecht, B. A., Widener, K. B., Moran, K. P., Luke, E.
580   P., Johnson, K. L., Bharadwaj, N., and Mead, J. B.: Development and applications of ARM
581   millimeter-wavelength cloud radars, Meteorological Monographs, 57, 17.11-17.19, 2016.
582   Lapple, C., and Shepherd, C.: Calculation of particle trajectories, Industrial & Engineering
583   Chemistry, 32, 605-617, 1940.
584   Lhermitte, R. M.: Centimeter & millimeter wavelength radars in meteorology, Lhermitte
585   Publications, 2002.
586   Li, H., and Moisseev, D.: Two layers of melting ice particles within a single radar bright band:
587   Interpretation and implications, Geophysical Research Letters, 47, e2020GL087499, 2020.
588   Luke, E. P., Kollias, P., Johnson, K. L., and Clothiaux, E. E.: A technique for the automatic
589   detection of insect clutter in cloud radar returns, Journal of Atmospheric and Oceanic
590   Technology, 25, 1498-1513, 10.1175/2007jtecha953.1, 2008.
591   Luke, E. P., Kollias, P., and Shupe, M. D.: Detection of supercooled liquid in mixed-phase clouds
592   using radar Doppler spectra, Journal of Geophysical Research-Atmospheres, 115,
593   10.1029/2009jd012884, 2010.
594   Luke, E. P., Yang, F., Kollias, P., Vogelmann, A. M., and Maahn, M.: New insights into ice
595   multiplication using remote-sensing observations of slightly supercooled mixed-phase clouds in
596   the Arctic, Proceedings of the National Academy of Sciences, 118, e2021387118, 2021.
597   Maahn, M., Loehnert, U., Kollias, P., Jackson, R. C., and McFarquhar, G. M.: Developing and
598   Evaluating Ice Cloud Parameterizations for Forward Modeling of Radar Moments Using in situ
599   Aircraft Observations, Journal of Atmospheric and Oceanic Technology, 32, 880-903,
600   10.1175/jtech-d-14-00112.1, 2015.
601   Mages, Z., Kollias, P., Zhu, Z., and Luke, E. P.: Surface-based observations of cold-air outbreak
602   clouds during the COMBLE field campaign, Atmospheric Chemistry and Physics Discussions, 1-
603   39, 2022.
604   Marshall, J. S., and Palmer, W. M. K.: The distribution of raindrops with size, Journal of
605   meteorology, 5, 165-166, 1948.
606   Mech, M., Maahn, M., Kneifel, S., Ori, D., Orlandi, E., Kollias, P., Schemann, V., and Crewell, S.:
607   PAMTRA 1.0: the Passive and Active Microwave radiative TRAnsfer tool for simulating
608   radiometer and radar measurements of the cloudy atmosphere, Geoscientific Model
609   Development, 13, 4229-4251, 2020.

610   Mie, G.: Beiträge zur Optik trüber Medien, speziell kolloidaler Metallösungen, Annalen der
611   physik, 330, 377-445, 1908.
612   Moisseev, D. N., and Chandrasekar, V.: Polarimetric spectral filter for adaptive clutter and noise
613   suppression, Journal of Atmospheric and Oceanic Technology, 26, 215-228, 2009.
614   Mróz, K., Battaglia, A., Kneifel, S., von Terzi, L., Karrer, M., and Ori, D.: Linking rain into ice
615   microphysics across the melting layer in stratiform rain: a closure study, Atmospheric
616   Measurement Techniques, 14, 511-529, 2021.
617   Nijhuis, A. C. O., Yanovsky, F. J., Krasnov, O., Unal, C. M., Russchenberg, H. W., and Yarovoy, A.:
618   Assessment of the rain drop inertia effect for radar-based turbulence intensity retrievals,
619   International Journal of Microwave and Wireless Technologies, 8, 835, 2016.
620   Oue, M., Kollias, P., Ryzhkov, A., and Luke, E. P.: Toward exploring the synergy between cloud
621   radar polarimetry and Doppler spectral analysis in deep cold precipitating systems in the Arctic,
622   Journal of Geophysical Research: Atmospheres, 123, 2797-2815, 2018.
623   Oue, M., Tatarevic, A., Kollias, P., Wang, D., Yu, K., and Vogelmann, A.: The Cloud-resolving
624   model Radar SIMulator (CR-SIM) Version 3.3: description and applications of a virtual
625   observatory, Geoscientific Model Development (Print), 13, 2020.
626   Pruppacher, H. R., and Beard, K.: A wind tunnel investigation of the internal circulation and
627   shape of water drops falling at terminal velocity in air, Quarterly Journal of the Royal
628   Meteorological Society, 96, 247-256, 1970.
629   Schlichting, H., and Kestin, J.: Boundary layer theory, Springer, 1961.
630   Shinozuka, M., and Deodatis, G.: Simulation of stochastic processes by spectral representation,
631   1991.
632   Silber, I., Jackson, R. C., Fridlind, A. M., Ackerman, A. S., Collis, S., Verlinde, J., and Ding, J.: The
633   Earth Model Column Collaboratory (EMC 2) v1. 1: an open-source ground-based lidar and radar
634   instrument simulator and subcolumn generator for large-scale models, Geoscientific Model
635   Development, 15, 901-927, 2022.
636   Wang, D., Bartholomew, M. J., Giangrande, S. E., and Hardin, J. C.: Analysis of Three Types of
637   Collocated Disdrometer Measurements at the ARM Southern Great Plains Observatory, Oak
638   Ridge National Lab.(ORNL), Oak Ridge, TN (United States). Atmospheric …, 2021.
639   Williams: Vertical air motion retrieved from dual-frequency profiler observations, Journal of
640   Atmospheric and Oceanic Technology, 29, 1471-1480, 2012.
641   Williams, C. R., Maahn, M., Hardin, J. C., and de Boer, G.: Clutter mitigation, multiple peaks, and
642   high-order spectral moments in 35 GHz vertically pointing radar velocity spectra, Atmospheric
643   Measurement Techniques, 11, 4963-4980, 10.5194/amt-11-4963-2018, 2018.
644   Yanovsky, F.: Simulation study of 10 GHz radar backscattering from clouds, and solution of the
645   inverse problem of atmospheric turbulence measurements, IEE Conference Publication, 1996,
646   188-193,
647   Zhao, N., Huang, G., Kareem, A., Li, Y., and Peng, L.: Simulation of ergodic multivariate
648   stochastic processes: An enhanced spectral representation method, Mechanical Systems and
649   Signal Processing, 161, 107949, 2021.
650   Zhu, Z., Kollias, P., Yang, F., and Luke, E.: On the estimation of in‐cloud vertical air motion using
651   radar Doppler spectra, Geophysical Research Letters, 48, e2020GL090682, 2021.

652   Zhu, Z., Kollias, P., Luke, E., and Yang, F.: New insights on the prevalence of drizzle in marine

653   stratocumulus clouds based on a machine learning algorithm applied to radar Doppler spectra,

654   Atmospheric Chemistry and Physics, 22, 7405-7416, 2022.

655

656